CrystEngComm

Accepted Manuscript

ROYAL SOCIETY OF CHEMISTRY

www.rsc.org/crystengcomm

CrystEngComm RSCPublishing

ARTICLE

Graphene Oxide-assisted Synthesis and Photocatalytic Hydrogen Production of Mix-phase Titanium Dioxide (TiO_2) Nanosheets

Cite this: DOI: 10.1039/x0xx00000x

Received 00th January 2012,
Accepted 00th January 2012

DOI: 10.1039/x0xx00000x

www.rsc.org/

Fanpeng Cai,[a, b] Yubin Tang,[b] Hao Shen,[c] Chao Wang,[a] Ao Ren,[a] Lisong Xiao,[a] Wei Gu,[a] Weidong Shi[a,*]

Novel mix-phase TiO_2 nanosheets were successfully synthesized by a facile Sol-gel method via using graphene oxide (GO) as the sacrifice template for the first time. The SEM, TEM and AFM images revealed that the thickness of mix-phase TiO_2 nanosheets was ca. 66 nm, and the TiO_2 nanosheets were in a polycrystalline phase and made up of nanoparticles with the diameters of 15-25 nm. In addition, we observed that the proportion of rutile and anatase changed with the amount of tetrabutyltitanate (TBT). The results showed that the sample with 4 mL tetrabutyltitanate (TBT-4) exhibited the highest hydrogen production rate (339 μmol/h) in all samples, which was 47% higher than the bulk sample. It was mainly attributed to the surface phase junction of anatase and rutile and the special morphology of the samples.

Keywords: mix-phase TiO_2 nanosheets, Sol-gel method, hydrogen production, graphene oxide as the template

1 Introduction

Energy and environmental issues at a global level caused by the burning of fossil fuels are important topics. It is urgent to construct new energy systems in order to solve these issues. Hydrogen as an ultimately clean energy provides an ideal alternative to replace fossil fuels. Photocatalytic water splitting is a promising approach to directly converting solar energy into hydrogen energy by producing H_2 from water [1]. Since water and sunlight are naturally abundant, the photocatalytic water splitting is considered to be economically viable to produce hydrogen energy.

Among semiconductor catalysts with the ability of assist H_2 production from water splitting, TiO_2 is the most promising candidate due to its super-high activity, chemical stability, non-toxicity and low cost [2-5]. To the best of our knowledge, the surface phase junction plays an important role in photocatalytic hydrogen production rate [6]. There have been many researchers and review articles showing that the photocatalytic hydrogen production rate of mix-phase TiO_2 is much higher than that of pure phase [7-12]. There were also researchers insisted that there was a synergetic effect exists in mix-phase TiO_2 [13, 14]. Bechstein et al. found that the mix-phase TiO_2 film with 60% anatase and 40% rutile exhibited optimal performance at a 50% enhanced activity compared with pure anatase [15]. Xu et al. proposed a hypothesis about the "intrinsic" photoactivity of mix-phase TiO_2 and the synergistic effect is mainly attributed to O_2 transfer from anatase phase to rutile [16]. All these researches have demonstrated that the surface phase junction greatly enhanced the photocatalytic performance of mix-phase TiO_2.

Furthermore, the photocatalytic activity of TiO_2-based semiconductor is greatly affected by their morphology, including shape, size, porosity and surface feature. For example, Xu et al. reported the morphology had an important influence on photocatalytic activity [17]. Their studies showed the photocatalytic activities of anatase TiO_2 nanocrystals change with facets exposed ratios. It is well reported that the 2D nanosheets have many unique advantages over other structures of photocatalysis such as the small weight, large surface area and the possession of more effective surface [18-23].

Up to now, the TiO_2 sheets were prepared by various methods. Han et al. synthesized anatase TiO_2 nanosheets with a high percentage of exposed (001) facets via a simple hydrothermal route [24]. And Gu et al. synthesized anatase TiO_2 nanosheets supported on reduced graphene oxide via a solvothermal method [25]. However, the fabrication of mix-phase TiO_2 nanosheets was limited by synthetic methods and the nature of materials. Therefore, it is not a surprise that no papers on the synthesis of mix-phase TiO_2 nanosheets have been reported to date. That makes the design of novel mix-phase TiO_2 nanosheets for photocatalytic hydrogen generation is still a challenge to meet the requirement in research.

Herein, we for the first-time report the synthesis of mix-phase TiO_2 nanosheets with controllable anatase and rutile contents by using GO as the template. The experimental result showed that the as-obtained mix-phase TiO_2 nanosheets exhibited excellent H2 production activities, indicating that the synergetic effect of mix-phase TiO_2 nanosheets plays an important role in the photocatalytic H_2 production rate.

2 Experimental

2.1. Chemicals

Flake graphite, H_2SO_4, HCl, P_2O_5 and $KMnO_4$ were purchased from Sinopharm (Beijing, China). H_2O_2, HAc, tetrabutyltitanate (TBT) and ethanol were purchased from Aladdin (Shanghai, China). All reagents were of analytical grade without further purification, and the deionized water was used in all experiments.

2.2. Synthesis of samples

Synthesis of GO: GO was synthesized from graphite by a modified Hummers method [26-29]. Firstly, a mixture of graphite (1 g), concentrated H_2SO_4 (6 ml, 98%), $K_2S_2O_8$ (2 g) and P_2O_5 (2 g) was heated at 80 °C for 5 h on a hotplate. The mixture was then cooled to room temperature and diluted with 200 ml water. After removing the acid by filtration and washing with water, this pre-oxidized graphite was dried in vacuum oven at 60 °C. The pre-oxidized graphite and 60 ml H_2SO_4 (98%) was put into a 500-ml flask in an ice-water bath. Then, 8 g $KMnO_4$ was added into the flask and the temperature of the water bath was increased to 35 °C and allowed to stand for 2 h. After the mixture was diluted with 250 ml water, 20 ml H_2O_2 was added into the flask. The solution turned yellow. The resulting graphite oxides were washed with HCl aqueous solution (1:10) to remove the acid and metal ions. Finally, the GO sheets were obtained by sonicating the graphite oxide.

Synthesis of GO@TiO_2 nanosheets: GO@TiO_2 nanosheets were synthesized according to Sol-gel process. 30 ml Acetic acid (HAc), tetrabutyltitanate (TBT) were added into a 250-ml beaker dropwise under vigorous stirring. The amount of TBT changes from 1 ml to 5 ml. After vigorous stirring 30 min in the room temperature, the GOs solutions (GOs dispersed in ethanol) were added into the beaker. After 6 h, the composites were washed with ethanol by repeated centrifugation and dried in a vacuum oven.

Synthesis of TiO_2 nanosheets: the GO@TiO_2 nanosheets were calcined at 600 °C in air for 6 h. The powder tuned to totally white from black after the calcination, indicating the removing of the GOs. The Schematic illustrations of the synthetic process of TiO_2 nanosheets were shown in Scheme. 1. The bulk sample was synthesized without GOs. In a typical procedure, 5 mL TBT droped wise in 30mL HAc to form a mix-solution, after stirring for 30 min, add 40 mL ethanol into the previous mix-solution and stirring for another 6h. Then the composites were washed with ethanol by repeated centrifugation and dried in a vacuum oven. After that, the composites were calcined at 500 °C in air for 6 h to obtain the high crystallized anatase TiO_2 particles.

Scheme. 1. Schematic illustrations of the synthetic process of TiO_2 nanosheets.

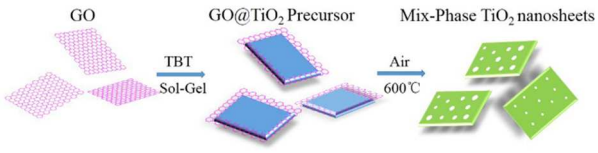

2.3. Characterization

The products were characterized by X-ray diffraction measurements carried out on X-ray diffractometer (XRD, Bruker D8 Advance diffractometer) with Cu-Kα radiation in the range of 5-80° at a scanning rate of 7°/min. Scanning electron microscopy (SEM) images were collected on an S-4800 field emission SEM (FESEM, Hitachi, Japan). Transmission electron microscopy (TEM) images were collected on an F20 S-TWIN electron microscope (Tecnvai G2, FEI Co.), using a 200 kV accelerating voltage. UV-vis diffused spectra of the products was obtained from a UV-vis spectrophotometer (UV2450, Shimadzu, Japan). $BaSO_4$ was used as a reflectance standard. Raman spectra was acquired on a Reflex Raman Microprobe (Renishaw inVia, England). Specific surface areas were calculated using the Brunauere-Emmette-Teller (BET) model via Micromeritics ASAP-2000 nitrogen adsorption apparatus. Atomic force microscope (AFM) images were collected on a park systermXE-120 (parkXE-120, park system, America). The photoluminescence spectra was obtained on a F4500 (Hitachi, Japan) photoluminescence detector. A Netzsch model STA 449 C thermal analyzer was used in the present investigation.

2.4. Photocatalytic hydrogen production

The photocatalytic hydrogen production experiments were carried out in a Lab-H_2 photocatalytic hydrogen production system. A 300W Xenon arc lamp was used as a light source and was positioned 20 cm away from the reactor in the system. In a typical photocatalytic experiment, 50 mg of the prepared TiO_2 photocatalyst was dispersed with constant stirring in 200 mL 20% methanol aqueous solution. Prior to irradiation, the system was vacuumized to remove the dissolved oxygen. During the whole reaction process, vigorous agitation was performed to ensure the uniform irradiation of the TiO_2 photocatalysts suspension. A certain amount of H_2PtCl_6•$6H_2O$ aqueous solution was dripped into the system to load 0.5 wt% Pt onto the surface of the photocatalyst by a photochemical reduction deposition method. The generated gas was collected intermittently through the septum, and hydrogen content was analyzed by the gas chromatograph (GC-SP7800, Beijing Jing Ke Ruida, China, TCD, nitrogen as a carrier gas and 5 Å molecular sieve column). All glassware was rigorously cleaned and carefully rinsed with distilled water prior to use.

3. Results and discussion

3.1. Structure and morphology

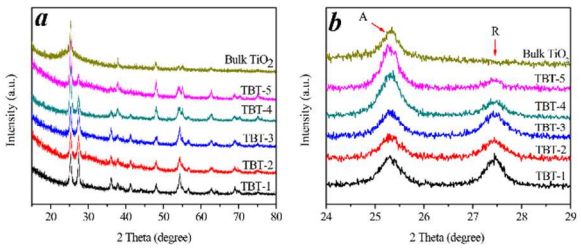

Fig. 1. a) XRD patterns of different quantity of TBT and bulk samples, b) the magnified XRD patterns in the range of 2θ=24° to 29°, A and R represent anatase and rutile, respectively.

A series of samples was synthesized by controlling different quantity of TBT with 1 mL, 2 mL, 3 mL, 4 mL and 5 mL, named as TBT-1, TBT-2, TBT-3, TBT-4 and TBT-5, respectively. The crystallographic structure and phase purity of all samples were examined by X-ray powder diffraction (XRD) studies. As shown in Fig. 1a, the XRD patterns of all samples can be indexed into mix-phase TiO_2. Particularly, as shown in the magnified XRD patterns in the range from 2θ=24° to 29° (Fig. 1b), the percentage of rutile phase decreased as the amount of TBT increased.

To be more specific, a commonly used method to determine the weight percentage of the rutile (W_R) portion in the mixture

of rutile and anatase was applied as shown in the following equation [30-32]:

$$W_R = \frac{A_R}{0.884A_A + A_R}$$

Here, the A_R stands for the integrated intensity of rutile (110) peak, and the A_A represents the integrated intensity of anatase (101) peak. When 1 mL TBT was added, the sample TBT-1 contained 47.8% anatase, and rutile 52.2%. While increased the TBT to 5 mL, the percentage of anatase increased to 81.1%, with only 18.9% of rutile remaining in the sample TBT-5. The detailed comparison for phase composition is summarized in Table 1. The XRD patterns of the sample before calcined was inserted in Fig. S2, which can be indexed into anatase phase with poor crystallinity.

Table 1 Summary of properties of samples synthesized from different amount TBT.

Sample ID	amount of TBT (mL)	Anatase %	Rutile %	Surface area (m^2/g)
TBT-1	1 mL	47.8	52.2	89
TBT-2	2 mL	49.9	51.1	91
TBT-3	3 mL	51	49	53
TBT-4	4 mL	69.4	31.6	59
TBT-5	5 mL	81.1	18.9	41

No GO peak was observed at 2°-10° in XRD patterns of all samples, indicating that GO has been removed in all samples. The GO's characteristic peaks in Raman spectra are D-band (1350 cm^{-1}) and G-band (1588 cm^{-1}), and they were not detected in the calcined samples (Fig. 2). The result is consistent with the removal of the GO in the process of calcination.

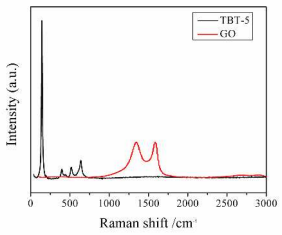

Fig. 2. Raman spectra of GO (red) and TBT-5 (black).

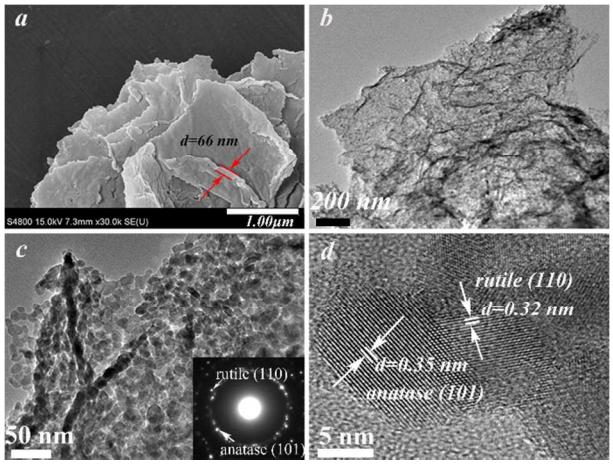

Fig. 3. a) the SEM image, b and c) the TEM image, d) the HRTEM image for TBT-4, respectively. The insert is SAED image for TBT-4.

The morphology and size of as-synthesized TiO_2 nanosheets were studied through the scanning electron microscope (SEM), transmission electron microscope (TEM) and high-resolution transmission electron microscope (HRTEM). As shown in the SEM image (Fig. 3a), TBT-4 sample is composed of numerous sheet structures with thickness of about 66 nm. The TEM image (fig. 3b) further reveals the sheet structure of TBT-4 sample with near transparent appearance and wrinkles on the surface. As can be seen in the higher magnification (Fig. 3c), the as-prepared TiO_2 nanosheets presented in a polycrystalline phase and assembled by well-dispersed 15-25 nm nano-particles. The selected area electron diffraction (SAED) pattern (inset of Fig. 3c) can be indexed to the anatase TiO_2 (101) and rutile TiO_2 (110) diffractional rings, which reveals the polycrystalline nature of nanosheets and confirms that the nanosheets contain anatase and rutile TiO_2. The corresponding HRTEM image (Fig. 3d) showed clear lattice fringes on the edge, which correspond to the (101) plane of anatase TiO_2 phase with interplanar spacing d = 0.35 nm and the (110) plane of rutile TiO_2 phase with interplanar spacing d = 0.32 nm, respectively. This result is in good agreement with the XRD analysis and selected area electron diffraction (SAED) pattern. Low magnification SEM and TEM images of TBT-4 sample (Fig. S3) were also provided to demonstrate the sheet structure and graphene-like morphology of our sample.

In our present work, we obtain TiO_2 nanosheets by a facile Sol-gel method with GO as the sacrifice template. Because of the distribution of carboxyl groups on the surface of GO, theTiO_2 precursor dispersed on the carbon support and were eager to accumulate along the carboxyl groups. After Sol-gel process, layered TiO_2 precursor covered on the surface of GO. This process was shown in Fig.S1. As a result, change the dosage of TBT may obtain TiO_2 nanosheets with different thickness. In order to confirm the fact, we provide TEM images (Fig.S4) of all other samples in the supporting information. No obvious morphological difference among these samples with different TBT amounts were observed.

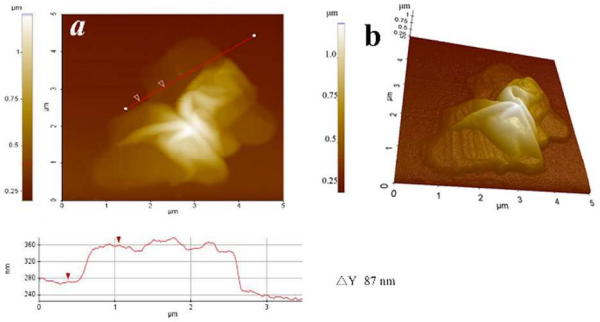

Fig. 4. a) AFM images of TBT-4 nanosheets, with the inset below showing the line profiles along the red line. b) The AFM 3D image of TBT-4.

In order to investigate the morphology and the thickness of the TiO_2 nanosheets, we study the materials using an atomic force microscope (AFM). Fig. 4a showed the 2D AFM images of TiO_2 nanosheets and its' line profiles along the red line. The red marker corresponds to TiO_2 nanosheets with a height of 87 nm. Fig. 4b shows 3D AFM micrographs of the TiO_2 nanosheets. Clearly the individual TiO_2 presented sheet's structure. And we can observe wrinkle-like features as graphene on the TiO_2 nanosheets. Basically, we can find the surface of TiO_2 nanosheets is very smooth.

It is well acknowledged that surface area is very important to the photocatalytic activity of TiO_2. The material templated by graphene oxide has an opportunity to possess huge specific surface area values. N_2 adsorption–desorption isotherms were recorded on ASAP 2020 instrument, from which the surface areas were calculated by applying the Brunauer-Emmett-Teller (BET) method. We listed the values of specific surface area of all samples in table 1. TBT-2 has the largest values of specific surface area (ca. 91 m^2/g), and TBT-5 has the smallest values of specific surface area (ca. 41 m^2/g). The relative large values of specific surface area may have a great impact on photocatalytic activity of as-prepared TiO_2.

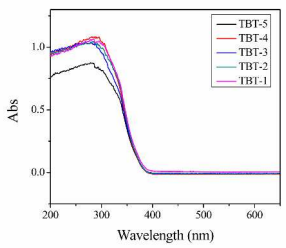

Fig. 5. The UV-vis absorption spectra of all samples.

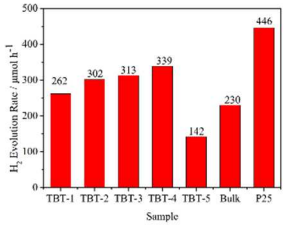

Fig. 6. Comparison of H_2 evolution rates of all samples using 20% methanol aqueous solution and 0.5 wt% Pt as a cocatalyst; a 300W xenon arc lamp was used as the light source.

3.2. Photocatalytic activity

Fig. 5 shows the UV-vis absorption spectrum of all samples. There was no significant increase of the absorption in the light absorption range. As shown in Fig. 5, with increasing the amount of TBT in the system, the absorption edge of the samples had no obviously shifts, reflecting that the band gap values of TiO_2 obtained were close. We have conducted the hydrogen production experiment, and the results were shown in Fig. 6. The TBT-4 (339 μmol/h) possess the highest hydrogen production rate whereas the TBT-5 (142 μmol/h) displays the lowest hydrogen production rate. As a comparison, the hydrogen production rate of bulk sample and P25 were 230 μmol/h and 446 μmol/h, respectively.

In generally, there are two major factors affecting the photocatalytic activity of TiO_2, including the A/R ratio and the surface area. On the one hand, Gang et al. reported that the work function of rutile is 0.2 eV lower than that of anatase, the electron affinity of anatase is higher than rutile[33, 37]. This would favor the transfer of photoexited electrons from rutile to anatase, and the transfer of holes from anatase to rutile at a clean interface, thereby effectively suppressing the recombination of photoexited electrons and holes [34, 35]. The reaction mechanism was thus briefly described in Scheme 2. Due to the effective charge separation, the synergetic effect between anatase and rutile leads to the high photocatalytic activity of mix-phase TiO_2 nanosheets [36, 37]. On the other hand, many studies have reported that the surface area of photocatalyst has a very strong effect on the photochemical reactive sites. In other words, the larger surface area, the more reactive sites contribute to the photochemical reaction [38, 39]. Wang et al. reported the ordered mesoporous TiO_2 with 163 m^2/g surface area showed the best photocatalytic activity among all samples, improved by 2.6 times as compared to the sample with 128 m^2/g surface area [40]. Owning to the large surface area and small particle size of P25, the hydrogen production rate is higher than TBT-4.

Scheme. 2. The reasonable photo-generated electron-hole conduction mechanism under a 300W Xenon arc lamp irradiation on TiO_2 surface phase junction.

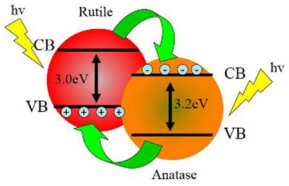

However, the surface area in our case was not the key factor affecting the photocatalytic hydrogen production rate. Specifically, from TBT-1 to TBT-4, the photocatalytic hydrogen production rate increased with the amount of anatase phases. This phenomenon implied that the A/R ratio played an important role in the photocatalytic hydrogen production of the mix-phase TiO_2 nanosheets rather than the surface area. Obviously, from TBT-1 to TBT-4, the synergetic effect between anatase and rutile to be responsible for the pretty high photocatalytic activity. For TBT-4, the amount of rutile was exactly suitable to assist electron-hole pair separation. This result could also be verified from photoluminescence emission (Fig. 7). In other words, too many rutile made the electron-hole recombination rate higher than the electron conductivity, thus, the photocatalytic hydrogen production rate was decreased with an increased in a rutile amount. That's why the photocatalytic hydrogen production rate of TBT-4 is higher than that of TBT-1, TBT-2 and TBT-3. It's also not surprise that the photocatalytic hydrogen production rate of TBT-4 is higher than that of pure anatase phase of bulk TiO_2. Nevertheless, for TBT-5, the photocatalytic hydrogen production rate had a dramatic decreased, which was attributed to the smallest specific surface area and the lowest rutile phase composition. That was to say the amount of rutile is insufficient to assist electron-hole pair separation. In addition, the 2D TiO_2 nanosheets structures also had a contribution to the photocatalytic hydrogen production rate, because sheet structures have more active sites than 0D and 1D structures and exhibit more effective surface than other structures [18, 19].

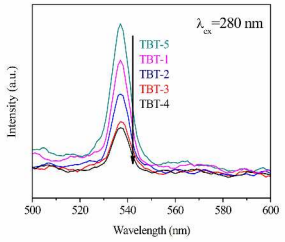

Fig. 7. The photoluminescence spectra of all samples (10mg were well-dispersed into 5 mL of ethanol) with excitation wavelength of 280 nm.

3.3. Photoluminescence spectra

The PL emission intensity is related to the recombination of excited electrons and holes, and thus, the lower emission intensity is indicative of a decrease in recombination rate and an increase the photocatalytic activity [41-43]. Photoluminescence (PL) emission spectra of all samples showed in Fig. 7. The measurement was conducted at the excitation wavelength of 280 nm with a photomultiplier tube voltage of 500 V. The PL spectra of all samples showed a broadband with a maximum around 536 nm. According to the PL results, the increase in the TBT amount caused a decrease in photoluminescence emission, although the band-gap energy did not change significantly (Fig. 5). This indicates the electron-hole recombination rate of TBT-4 was much lower than those of other samples. The result is consistent with the photocatalytic hydrogen production rate of all samples.

Conclusions

In summary, the novel TiO_2 nanosheets were successfully synthesized by a facile Sol-gel method with graphene oxide as the sacrifice template. The as-prepared TiO_2 nanosheets were in a polycrystalline phase which made up of nano-particles, and the nano-particles were dispersed with diameters of 15-25 nm. The results show that TBT-4 sample exhibits the highest hydrogen production rate (339 μmol/h) among all samples, which is 47% higher than the bulk sample. This is because the electron-hole recombination rate of TBT-4 was much lower than those of other samples, thus makes the photocatalytic hydrogen production rate much higher.

Acknowledgements

The authors are grateful for National Natural Science Foundation of China (21276116, 21301076, 21303074 and 21201085), Natural science foundation of Jiangsu Province (BK20131257, BK2012294), Special Financial Grant from the China Postdoctoral Science Foundation (2013T60501), Program for New Century Excellent Talents in University (NCET-13-0835), Henry Fok Education Foundation (141068) and Six Talents Peak Project in Jiangsu Province (XCL-025).

Notes and references

[a] School of Chemistry and Chemical Engineering, Jiangsu University, Xuefu Road 301, Zhenjiang, 212013, P. R. China.

[b] School of Biology and Chemical Engineering, Jiangsu University of Science and Technology, Zhenjiang, 212003, P. R. China.

[c] Institute of Inorganic Chemistry, University of Cologne, Greinstrasse 6, D-50939 Cologne, Germany.

*Corresponding author: Tel.: +86 511 8879 0187 Fax. : +86 511 8879 1108

E-mail address: swd1978@ujs.edu.cn(W. Shi)

1 A. Kudo and Y. Miseki, *Chemical Society reviews*, 2009, **38**, 253-278.
2 X. Chen and S. S. Mao, *Chemical reviews*, 2007, **107**, 2891-2959.
3 M. Addamo, V. Augugliaro, M. Bellardita, A. Paola, V. Loddo, G. Palmisano, L. Palmisano and S. Yurdakal, *Catalysis Letters*, 2008, **126**, 58-62.
4 R. Daghrir, P. Drogui and D. Robert, *Industrial & Engineering Chemistry Research*, 2013, 130226090752004.
5 H. B. Wu, H. H. Hng and X. W. Lou, *Advanced materials*, 2012, **24**, 2567-2571.
6 X. Wang, Q. Xu, M. Li, S. Shen, X. Wang, Y. Wang, Z. Feng, J. Shi, H. Han and C. Li, *Angewandte Chemie*, 2012, **51**, 13089-13092.
7 A. Zachariah, K. V. Baiju, S. Shukla, K. S. Deepa, J. James and K. G. K. Warrier, *Journal of Physical Chemistry C*, 2008, **112**, 11345-11356.
8 R. G. Nair, S. Paul and S. K. Samdarshi, *Solar Energy Materials and Solar Cells*, 2011, **95**, 1901-1907.
9 D. A. H. Hanaor, I. Chironi, I. Karatchevtseva, G. Triani and C. C. Sorrell, *Advances in Applied Ceramics*, 2012, **111**, 149-158.
10 H. Li, B. Xu and Y. Fan, *Chemical Physics Letters*, 2013, **558**, 66-71.
11 H. Tian, G. Zhao, Y.-n. Zhang, Y. Wang and T. Cao, *Electrochimica Acta*, 2013, **96**, 199-205.
12 M. Niu, D. Cheng and D. Cao, *The Journal of Physical Chemistry C*, 2014, 140305155820004.
13 T. Ohno, K. Sarukawa, K. Tokieda and M. Matsumura, *Journal of Catalysis*, 2001, **203**, 82-86.
14 D. C. Hurum, A. G. Agrios, K. A. Gray, T. Rajh and M. C. Thurnauer, *The Journal of Physical Chemistry B*, 2003, **107**, 4545-4549.
15 R. Su, R. Bechstein, L. Sø, R. T. Vang, M. Sillassen, B. Esbjörnsson, A. Palmqvist and F. Besenbacher, *The Journal of Physical Chemistry C*, 2011, **115**, 24287-24292.
16 S. Cong and Y. Xu, *The Journal of Physical Chemistry C*, 2011, **115**, 21161-21168.
17 J. Li, Y. Yu, Q. Chen, J. Li and D. Xu, *Crystal Growth & Design*, 2010, **10**, 2111-2115.
18 J. Liu and X. W. Liu, *Advanced materials*, 2012, **24**, 4097-4111.
19 E. L. Tae, K. E. Lee, J. S. Jeong and K. B. Yoon, *Journal of the American Chemical Society*, 2008, **130**, 6534-6543.
20 T. Huang and D. Qiu, *Langmuir : the ACS journal of surfaces and colloids*, 2014, **30**, 35-40.
21 Y. Li, D. Cao, Y. Liu, R. Liu, F. Yang, J. Yin and G. Wang, *International Journal of Hydrogen Energy*, 2012, **37**, 13611-13615.
22 L. Zhang, W. Wang, Z. Chen, L. Zhou, H. Xu and W. Zhu, *Journal of Materials Chemistry*, 2007, **17**, 2526.
23 X. Hu, X. Shen, R. Huang, Y. Masuda, T. Ohji and K. Kato, *Journal of Alloys and Compounds*, 2013, **580**, 373-376.
24 X. Han, Q. Kuang, M. Jin, Z. Xie and L. Zheng, *Journal of the American Chemical Society*, 2009, **131**, 3152-3153.
25 L. Gu, J. Wang, H. Cheng, Y. Zhao, L. Liu and X. Han, *ACS applied materials & interfaces*, 2013, **5**, 3085-3093.
26 Z. Lu, J. Zhu, D. Sim, W. Zhou, W. Shi, H. H. Hng and Q. Yan, *Chemistry of Materials*, 2011, **23**, 5293-5295.
27 C. Bao, L. Song, W. Xing, B. Yuan, C. A. Wilkie, J. Huang, Y. Guo and Y. Hu, *Journal of Materials Chemistry*, 2012, **22**, 6088.
28 W. Tu, Y. Zhou and Z. Zou, *Advanced Functional Materials*, 2013, **23**, 4996-5008.
29 E. V. Iski, E. N. Yitamben, L. Gao and N. P. Guisinger, *Advanced Functional Materials*, 2013, **23**, 2554-2564.
30 H. Zhang and J. F. Banfield, *The Journal of Physical Chemistry B*, 2000, **104**, 3481-3487.
31 F. Zuo, L. Wang and P. Feng, *International Journal of Hydrogen Energy*, 2014, **39**, 711-717.
32 J. G. Yu, J. C. Yu, M. K. P. Leung, W. K. Ho, B. Cheng, X. J. Zhao and J. C. Zhao, *Journal of Catalysis*, 2003, **217**, 69-78.
33 G. Xiong, R. Shao, T. C. Droubay, A. G. Joly, K. M. Beck, S. A. Chambers and W. P. Hess, *Advanced Functional Materials*, 2007, **17**, 2133-2138.
34 D. C. Hurum, K. A. Gray, T. Rajh and M. C. Thurnauer, *The journal of physical chemistry. B*, 2005, **109**, 977-980.
35 J. Zhang, Q. Xu, Z. Feng, M. Li and C. Li, *Angewandte Chemie*, 2008, **47**, 1766-1769.
36 P. Deák, B. l. Aradi and T. Frauenheim, *The Journal of Physical Chemistry C*, 2011, **115**, 3443-3446.
37 D. O. Scanlon, C. W. Dunnill, J. Buckeridge, S. A. Shevlin, A. J. Logsdail, S. M. Woodley, C. R. Catlow, M. J. Powell, R. G. Palgrave, I. P. Parkin, G. W. Watson, T. W. Keal, P. Sherwood, A. Walsh and A. A. Sokol, *Nature materials*, 2013, **12**, 798-801.
38 A. G. Prado and L. L. Costa, *Journal of hazardous materials*, 2009, **169**, 297-301.
39 A. T. Bell, *Science*, 2003, **299**, 1688-1691.
40 J. Wang, Z. Bian, J. Zhu and H. Li, *Journal of Materials Chemistry A*, 2013, **1**, 1296.

41 S. K. Choi, S. Kim, S. K. Lim and H. Park, *The Journal of Physical Chemistry C*, 2010, **114**, 16475-16480.
42 N. Murakami, Y. Kurihara, T. Tsubota and T. Ohno, *The Journal of Physical Chemistry C*, 2009, **113**, 3062-3069.
43 A. A. Ismail and D. W. Bahnemann, *Journal of Materials Chemistry*, 2011, **21**, 11686.

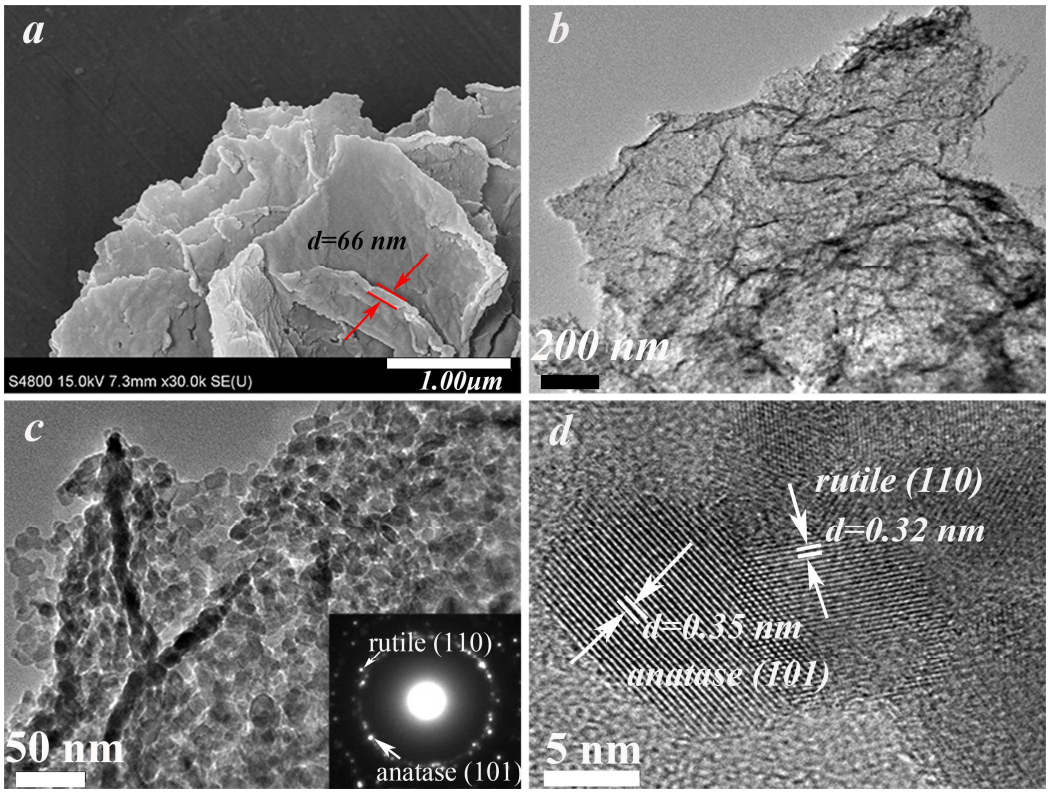

Fig. a) the SEM image, b and c) the TEM image, d) the HRTEM image for TBT-4, respectively. The insert is SAED image for TBT-4.